Revision 1

Correction1 12Nov2020

Carletonmooreite, Ni_3Si, a new silicide from the Norton County, aubrite meteorite

Laurence A.J. Garvie[1,2], Chi Ma[3], Soumya Ray[2], Kenneth Domanik[4], Axel Wittmann[5], and Meenakshi Wadhwa[2].

[1]Center for Meteorite Studies, [2]School of Earth and Space Exploration, Arizona State University, 781 East Terrace Rd., Tempe, AZ 85287-6004, USA (lgarvie@asu.edu). [3]Division of Geological and Planetary Sciences, California Institute of Technology, 1200 East California Boulevard, Pasadena, CA 91125, USA, [4]Lunar and Planetary Laboratory, University of Arizona, 1415 N 6th Ave, Tucson, AZ 85705,[5]Eyring Materials Center, Arizona State University, Tempe, AZ 85287, USA.

Abstract

Carletonmooreite (IMA 2018-68), Ni_3Si, is a new nickel silicide mineral that occurs in metal nodules from the Norton County aubrite meteorite. These nodules are dominated by low-Ni iron (kamacite), with accessory schreibersite, nickelphosphide, perryite, and minor daubréelite, tetrataenite, taenite, and graphite. The chemical composition of the holotype carletonmooreite determined by wavelength-dispersive electron-microprobe analysis is (wt%) Ni 82.8±0.4, Fe

4.92±0.09, and Si 13.08±0.08 (n=6, total = 100.81) giving an empirical formula of $(Ni_{2.87}Fe_{0.18})_{\Sigma=3.05}Si_{0.95}$, with an end-member formula of Ni_3Si. Further grains discovered in the specimen after the new mineral submission extend the composition, i.e., (wt%) Ni 81.44±0.82, Fe 5.92±0.93, Cu 0.13±0.02, and Si 13.01±0.1 (n=11, total = 100.51±0.41), giving an empirical formula $(Ni_{2.83}Fe_{0.22}Cu_{0.004})_{\Sigma=3.05}Si_{0.95}$. The backscattered electron-diffraction patterns were indexed by the *Pm*-3*m* auricupride ($AuCu_3$)-type structure and give a best fit to synthetic Ni_3Si, with a = 3.51(1) Å, V = 43.2(4) $Å^3$, Z = 1, and calculated density of 7.89 g/cm^3. Carletonmooreite is silver colored with an orange tinge, isotropic, with a metallic luster and occurs as euhedral to subhedral crystals 1 × 5 μm to 5 × 14 μm growing on tetrataenite into kamacite. The dominant silicide in the Norton County aubrite metal nodules is perryite $(Ni,Fe)_8(Si,P)_3$, with carletonmooreite restricted to localized growth on rare plessite fields. The isolated nature of small euhedral carletonmooreite single crystals suggests low-temperature growth via solid-state diffusion from the surrounding kamacite and epitaxial growth on the tetrataenite. This new mineral is named in honor of Carleton B. Moore, chemist and geologist, and founding director of the Center for Meteorite Studies at Arizona State University, for his many contributions to cosmochemistry and meteoritics.

Introduction

Aubrites are achondrite meteorites that are mostly pyroxenites dominated by nearly FeO-free enstatite with lesser amounts of plagioclase, diopside, forsterite, and accessory metals, sulfides, phosphides, and other phases (Keil 2010 Most of the aubrites are regolith impact brecciated pyroxenites and all formed under highly reducing conditions (Keil 2010). They have igneous origins and underwent fractional differentiation under highly reducing conditions (Keil 2010). Under these formation conditions, elements that are normally lithophile, such as Ti, Ca, and Na, become chalcophile, and Si behaves partly as a siderophile and occurs in the metal. Examples of minerals from the aubrites that form only under highly reducing conditions and do not occur on the surface of the Earth include heideite $FeTi_2S_4$, caswellsilverite $NaCrS_2$, oldhamite CaS, perryite $(Ni,Fe)_5(Si,P)_2$, and Ti-Cr-rich troilite (e.g., Keil 2010 and references therein). The Norton County aubrite is arguably the most studied meteorite of this class, in part because of the large 1 ton-mass that was recovered from the February 18th, 1948 fall over Kansas and Nebraska (La Paz 1948; Leonard 1948). To date, 25 minerals have been recorded from the Norton County meteorite and it is the type locality for caswellsilverite, cronusite $Ca_{0.2}CrS_2 \cdot 2H_2O$, and schöllhornite $Na_{0.3}CrS_2 \cdot H_2O$.

Metallic Fe-Ni is a minor component in the aubrites and occurs in a range of petrographic relationships from sub-micron to cm-sized nodules (Casanova et al. 1993). Possible origins for the metal include formation through in-situ reduction, incorporation via impacts, fragments of fractionally crystallized core, or trapped metal from a silicate+metal+sulfide magma (Casanova et al. 1993). Based in part on elemental and isotopic data, Ray et al. (2020) concluded that the Si-

bearing metal likely represents an incompletely segregated metal fraction formed during partial melting on the aubrite parent body. The Norton County metals have received scientific attention, in part because of their unusual chemical composition and because they host perryite, an Fe-Ni silicide phosphide (Wai 1970; Wasson and Wai 1970; Okada et al. 1991). Other minerals in the metal nodules include schreibersite, daubréelite, caswellsilverite, and graphite (Garvie et al. 2018). Unlike many meteoritic metals, a typical Widmanstätten pattern of kamacite and taenite is not present. Instead, many of the metal nodules show a prominent pseudo-Widmanstätten pattern delineated by laths of perryite (Wai 1970; Garvie et al. 2018).

During our elemental, mineralogical, and isotopic investigations of the metal nodules from Norton County (Garvie et al. 2018; Ray et al. 2020), we discovered a new Ni silicide. This mineral was submitted to the International Mineralogical Association (IMA) and approved as carletonmooreite (IMA 2018-68); its occurrence and characteristics are described here. The name is in honor of Carleton B. Moore, chemist and geologist, and founding director of the Center for Meteorite Studies at Arizona State University, for his many contributions to cosmochemistry and meteoritics. The holotype specimen is in the Carleton B. Moore Meteorite Collection of the Center for Meteorite Studies, Arizona State University, Tempe, Arizona 85287, USA.

Methods

A 13.32 g metal nodule from the Norton County aubrite (designated NC12 and is accessioned in the Center for Meteorite Studies as #523_C6a) was sectioned, mounted in epoxy, polished and gently etched with nital. The sample was analyzed with optical microscopy and scanning electron microscopy (SEM) imaging, electron probe microanalysis (EPMA) with wavelength

dispersive spectroscopy (WDS), and electron backscatter diffraction (EBSD). Carletonmooreite was discovered during our research on the Norton County metal nodules using the CAMECA SX100 electron microprobe in the Michael J. Drake Electron Microprobe lab at the University of Arizona (UofA). Subsequent analyses were undertaken with the JEOL JXA-8530F Hyperprobe in the Eyring Materials Center at Arizona State University (ASU), and the JEOL 8200 electron microprobe at the California Institute of Technology (Caltech).

The type specimen analyses for the new mineral classification were performed with the JEOL 8200 electron microprobe (15 kV and 10 nA, ~100 nm focused beam) at Caltech (Table 1). The interaction volume for X-ray generation in carletonmooreite is ~800 nm in diameter, estimated using the Monte Carlo simulation of electron trajectories. Standards used for calibration were pure metals for Fe, Ni, and Si Analyses were processed with the CITZAF correction procedure.

Additional analyses of carletonmooreite were undertaken with the JEOL JXA-8530F Hyperprobe (12 kV and 50 nA, focused beam) in the Eyring Materials Center at ASU (Table 2). Monte Carlo simulations of electron trajectories indicate a half-spherical X-ray excitation volume with a radius of ~500 nm for these analytical conditions. Standards used for calibration were pure metals for Fe, Co, Cu, Ni, Si, and schreibersite for P. This analytical protocol provided detection limits of 0.02 wt% for Si, P, and Co, 0.03 wt% for Fe, and 0.04 wt% for Cu and Ni. X-ray intensity maps were acquired using an accelerating voltage of 20 kV, beam current of 100 nA, a dwell time of 20 nA, and a beam diameter of 1 μm. Data acquisition and processing at ASU was done with the Probe for EPMA software by Probe, Inc., using the PAP algorithm for ZAF correction (Pouchou and Pichoir 1991)

Metal, perryite, and schreibersite with and surrounding the carletonmooreite were analyzed with a CAMECA SX100 electron microprobe (15 kV, 40 nA) in the Michael J. Drake Electron

Microprobe lab at UofA (Table 3). Standards used for calibration were pure metals for Fe, Ni, Co, Cr, Si, P in InP, and Cu in chalcopyrite. The bulk elemental analyses were acquired as the average of 195 data points across the metal nodule. Each data point was acquired using a 20-μm-diameter beam.

Single-crystal electron backscatter diffraction (EBSD) analyses were performed at Caltech using methods described in Ma and Rossman (2008, 2009). An HKL EBSD system on a ZEISS 1550VP Field-Emission SEM, was operated at 20 kV and 6 nA in focused beam mode with a 70º tilted stage and in a variable pressure mode (25 Pa). The variable pressure mode was used since the carbon coating was removed for better EBSD analysis. The focused electron beam was several nanometers in diameter. The spatial resolution for diffracted backscatter electrons is ~30 nm. The EBSD system was calibrated using a single-crystal silicon standard. The structure was determined and cell constants obtained by matching the experimental EBSD patterns with known structures of Ni-Si and Fe-Si phases (Lashko, 1951; Toman, 1952; Beck et al., 1973; Ochiai et al., 1984, Rabadanov and Ataev 2002; Schuette et al., 2003; Perez et al., 2004).

Occurrence, Chemistry, and Crystallography

The low-magnification optical image of the metal nodule section (2.2 × 1.6 cm) shows an aggregate of 1-cm- to mm-sized kamacite grains (Fig. 1a), locally separated by elongated, anhedral and rounded grains of schreibersite, and less commonly daubréelite and Ti-Cr-bearing troilite. The relative orientations of the kamacite grains are shown by the pseudo-Widmanstätten pattern formed by perryite laths that show three prominent sets of lamellae that sub-divide the grains into trapezoidal regions, and the abundant Neumann bands. Light diffracting from the oriented Neumann bands and perryite produce a rainbow effect on the etched metal (Fig. 1a).

Multiple sections through the nodule show several plessitic structures up to 2 mm wide, which under low-magnification optical imaging show an outer dark rim, inner bright zone, and central dark etched region. The section through the aubrite metal imaged in Figure 1a contains two plessitic regions – Pl1 (Fig. 1b) and Pl2 (Fig. S1). Carletonmooreite was discovered through element mapping of plessitic region Pl1 (Fig. 2), and the new mineral description was based on the data acquired from these grains (Table 1, Fig. 2a). Thus, most of the petrographic description is based on plessitic region Pl1. Subsequent analyses revealed carletonmooreite is also associated with plessitic region Pl2 (Fig. S2).

Elemental X-ray intensity maps of the plessitic region Pl1 show a high Ni (up to 50.1 wt%) rim that decreases to ~20 wt% near the center. WDS X-ray intensity maps for Fe, Ni, Si, and P (Fig. 2) clearly reveal the structural and elemental complexity of this triangular region surrounded by the perryite-rich kamacite. The microstructure of the plessite consists of several zones visible by optical microscopy (Fig 2a) and by element profiles (Fig. 3). From the Ni-rich border to the center of the plessite, an outer taenite rim (OTR), cloudy zone (CZ), clear taenite (CT), and martensite (M1 and M2) are visible. The interior of the plessite exhibits a lath-like structure that compared to the surrounding material is dark under BSE imaging and the etched section viewed under optical microscopy, with Ni contents ranging from 10.4 to 50.1 wt%, with a mean of 29.8 wt% based on the average of 113 data points. The composition of the OTR is consistent with tetrataenite [$Fe_{48.6}Cu_{0.4}Si_{1.3}Ni_{49.6}$ (at%)]. The taenite in the CT rim is $Fe_{79.5}Co_{0.2}Si_{1.2}Ni_{19.1}$ (in at%), with Co instead of Cu.

The triangular sides of the plessite Pl1 show regions with a planar interface between the kamacite and OTR and areas that are embayed into the OTR-CZ-CT boundary. The WDS X-ray intensity maps show that the embayed regions host perryite whereas regions of the planar OTR

show adhering grains that contain Ni, Fe, and Si, but lack the P characteristic of perryite (Fig. 2). These Ni-Fe-Si grains occur as euhedral-to-subhedral crystals that protrude up to 5 μm perpendicular to the outer taenite rim into the kamacite and up to 14 μm wide parallel to this boundary (Fig. 2): these are the holotype crystals of carletonmooreite (IMA 2018-68). Elemental WDS analysis of the grains from plessite Pl1 show the major elements Ni, Fe, and Si (Table 1). Phosphorous and cobalt concentrations are below the detection limit in carletonmooreite as measured by WDS. The empirical formula (based on 4 atoms *pfu*) is $(Ni_{2.87}Fe_{0.18})Si_{0.95}$. The end-member formula is Ni_3Si, which requires Ni 86.25 and Si 13.75.

Subsequent analyses of grains along plessite Pl1 and on Pl2 discovered in the specimen after the new mineral submission (see arrowed grains in Fig. S2) extend the composition (Table 2), giving an empirical formula $(Ni_{2.85}Fe_{0.20}Cu_{0.004})_{\Sigma=3.05}Si_{0.95}$ for four grains in Pl1 and $(Ni_{2.81}Fe_{0.25}Cu_{0.004})_{\Sigma=3.05}Si_{0.94}$ for two grains in plessite Pl2. These analyses overlap those in Table 1, though the Fe content of the two grains analyzed along Pl2 are slightly higher. The relatively low Fe content in the Ni_3Si is consistent with the experimental data that shows low solubility of Fe in Ni-Si silicides (Ackerbauer et al. 2009).

In reflected light, the mineral is silver colored with an orange tinge, exhibits a metallic lustre, and is isotropic. Streak, hardness, tenacity, cleavage, fracture, density, and optical properties could not be determined because of the small grain sizes. Density (calc.) = 7.89 $g \cdot cm^{-3}$ using the empirical formula Ni_3Si.

The EBSD patterns were indexed by the *Pm*-3*m* auricupride ($AuCu_3$)-type structure and give a best fit to the synthetic Ni_3Si cells from Lashko (1951), Beck et al. (1973) and Ochiai et al. (1984) (Fig. 4), with a mean angular deviation of 0.30º - 0.35º, revealing the following cell parameters: cubic, a = 3.51(1) Å, space group: *Pm*-3*m*, V = 43.2(4) $Å^3$, Z = 1. The EBSD patterns

revealed that the carletonmooreite crystals in Fig. 2a all have the same orientation with respect to each other, as revealed by their similar EBSD patterns. X-ray powder diffraction data (Table S1) in Å for Cu*K*α1, Bragg-Brentano geometry, were calculated with the empirical formula from this study, using Powder Cell version 2.4.

Discussion

The petrography and chemistry of twelve metal nodules from the Norton County aubrite, ranging in size from ~1 mm to 2 cm in the longest dimension (and varying in mass from 0.7 to >13.3 g) were studied, of which ten are Si-rich (Ray et al. 2020). These Si-rich nodules have similar textures and structures, but have a range of Si contents and δ^{56}Fe isotopic values (Garvie et al. 2017, 2018; Ray et al. 2019a,b, 2020). Characteristic of these metals is the Si content of the kamacite, which ranges from 0.25 to 1.83 wt% (Garvie et al. 2017, 2018). Perryite is visible and abundant across the whole of the polished and nital-etched surfaces of the Si-rich nodules. One of the largest nodules, designated NC12, contains plessitic structures on which the new mineral carletonmooreite was discovered. A WDS spot measurement traverse from the kamacite and into one of the plessites (Fig. 3) shows the characteristic Ni profile from the kamacite into the plessite, with Ni reaching a maximum near 50 wt% at the kamacite/tetrataenite boundary. As previously shown (Casanova et al. 1993), silicon broadly correlates with Ni content, though our high spatial resolution study shows that the Si content drops from around 0.33 wt% in the kamacite to 0.24 wt% at the kamacite/OTR boundary forming an "Si well" in the kamacite (Fig. 3b). The Si content then rises steadily and reaches a maximum ~15 μm beyond the kamacite/OTR boundary. The carletonmooreite crystals formed in the "Si well" directly attached to the OTR. In contrast, the perryite on the plessite has disrupted the planarity of the tetrataenite

and has formed within the embayed region from the Ni in the tetrataenite. In addition, there is an ~10 μm thick rim around the OTR that is largely devoid of perryite precipitates (Fig. 2).

Plessite Pl1 occurs between two differently oriented kamacite grains – K1 and K2 (Fig. 1b and 5). These orientations are revealed by the relative directions of the perryite laths in the kamacite, which form four directions in the two kamacite grains (Fig. 5) and directions of the prominent Neumann bands (Fig. 1b). The traditional view is that these laths form a pseudo-Widmanstätten pattern consistent with perryite precipitated on the $\{111\}_\gamma$ planes during cooling, similar to the patterns observed in iron meteorites (Yang and Goldstein, 2005). Alternatively, Buchwald (1975, p 663) suggested that the perryite may have exsolved on the $(111)_\alpha$ planes of kamacite, and not a taenite crystal. A third explanation is discussed below with perryite exsolving along the $(111)_{a2}$ planes, where α_2 is bcc martensite.

Nodule NC12 is estimated to have equilibrated within the aubrite parent body at 1310° C (Ray et al. 2020). This temperature is below the liquidus for pure Fe-Ni and the metal nodule would be taenite γ-Fe-Ni, which has the austenite fcc structure. Further cooling below ca. 900 °C initiates a solid-state transformation into the kamacite (bcc ferrite) stability field, in which a Widmanstätten pattern can form (Goldstein et al. 2009). For most irons, the formation of the Widmanstätten pattern is determined by the bulk Ni and P content and hence the path through the ternary Fe-Ni-P phase diagram as the planetesimal cools. The NC12 nodule is polycrystalline kamacite (Fig. 1a) suggesting that the original γ – taenite was itself polycrystalline. Schreibersite "stringers" and elongated anhedral grains are locally abundant between the kamacite grains. The occurrence of these intergranular schreibersites suggest that upon cooling the metal first entered the $\gamma_p \rightarrow \gamma_p$ + Ph stability field, (γ_p is the parent taenite and Ph is precipitated phosphide), with precipitation of schreibersite along the taenite grain boundaries.

The P content of the metal has a significant effect on the formation of the Widmanstätten pattern in iron meteorites (Yang and Goldstein 2005). In typical irons with roughly the same Ni and P compositions as nodule NC12, i.e., 8.1 wt% Ni and 0.1 wt% P, the cooling iron is expected to form a Widmanstätten pattern according to γ_p -> α_2 + γ_p -> α + γ_p (mechanism V in Yang and Goldstein, 2005), where γ_p is the parent taenite and α_2 is bcc martensite. An example of an iron with ~8 wt% Ni and low P is Muonionalusta (IVA), which displays a well-developed Widmanstätten pattern. However, nodule NC12 does not display such a pattern indicating that as the iron nodule cooled, the presence of Si in the metal initiated formation of Ni-bearing perryite prior to γ_p -> α_2 + γ_p, thus preventing formation of a Ni-rich γ phase. The perryite displays orientations consistent with its formation along the $\{111\}_\gamma$ planes, which suggests the following mechanisms: γ_p –> γ_p + Ph –> α_2 –> α + perryite. The formation of α_2 is initiated at M_s, which is the martensite starting temperature and is crystallographically related to γ_p (Yang and Goldstein 2005). However, the plessite fields in NC12 have high Ni contents (Fig. 3) that are significantly higher than that of the bulk metal. Plessite with such high Ni contents is not consistent with mechanism V and is best explained through another process called mechanism IV (Yang and Goldstein 2005).

On cooling, mechanism IV proceeds according to γ_p -> α_2 -> α + γ_n (Yang and Goldstein 2005). The new taenite (γ_n) that forms by this mechanism is significantly enriched in Ni compared to the surrounding metal, similar to that measured for the NC12 plessites (Fig. 3). The formation of the scattered plessite in NC12 is likely dependent on local Ni content of the γ_p phase. The microstructure and composition of the NC12 cores match that of duplex plessite (Zhang et al. 1993), which forms through martensite decomposition at martensite lath boundaries to a micro-structure of tetrataenite precipitates in a kamacite matrix. According to the Fe-Ni

phase diagram, these structures formed during cooling through the Fe-Ni phase diagram from ~450° C to below ~200° C (Zhang et al. 1993). Formation of the carletonmooreite would start at a maximum temperature when γ_n forms according to α_2 -> $\alpha + \gamma_n$ of mechanism IV, estimated to start near 600 °C and complete below ~300 °C. There are several possibilities for the formation of the perryite during mechanism IV, i.e., precipitated directly in the parent taenite according to γ_p -> γ_p + perryite followed by γ_p -> α_2 -> $\alpha + \gamma_n$. Alternatively, α_2 -> α_2 + perryite prior to further cooling and transformation to $\alpha + \gamma_n$. In the former case, the perryite will precipitate along the $\{111\}_\gamma$ whereas in the latter scenario it would precipitate along $\{111\}_{\alpha 2}$.

The outer edge of the plessite in contact with the kamacite shows planar and embayed regions (Fig. 2), and the distribution and identity of the silicides along this contact give insights into their formation. Perryite that formed within the embayed margins appears to have replaced the Ni-rich OTR, whereas the carletonmooreite only forms on the planar OTR and protrudes into the kamacite (Fig. 2). The embayed margins with rims of perryite suggest that its Ni is derived from the tetrataenite either concurrent with the plessite growth or by replacement post growth. However, the isolated nature of small euhedral carletonmooreite single crystals on the OTR suggests low-temperature growth via diffusion from the surrounding kamacite. Further evidence for late-stage diffusional growth of carletonmooreite together with epitaxial growth is revealed through EBSD data. The carletonmooreite crystals in Fig. 2 all have the same crystallographic orientation, which is the same as the underlying tetrataenite.

Ray et al. (2020) examined the chemistry and petrography of ten Si-rich metal nodules from the Norton County aubrite, though no other occurrences of carletonmooreite were encountered. Whereas perryite is abundant in all of the Si-rich nodules, only the nodule studied here (NC12) contained plessitic regions, despite the fact that other nodules, such as NC11,

contained similar Ni and P contents. The absence of carletonmooreite in the other nodules points to the importance of the localized crystal-chemical constraints imposed by the plessite.

Implications

Carletonmooreite joins a small but growing family of silicides with 11 members described to date (Ross et al. 2019). The majority are Fe-rich, while only perryite and carletonmooreite are Ni-rich (Ross et al. 2019). Many of these silicides have the potential to provide insights into parent body processes. For example, many of the silicides in polymict ureilites indicate short-lived, high-temperature processes in the near-surface environment of the parent asteroid. Other known Fe-silicides, such as luobusaite $Fe_{0.83}S_2$, linzhiite $FeSi_2$, and naquite FeSi, provide insights into terrestrial processes.

There are currently 5636 valid mineral species (as of September 2020) recorded by the Commission on New Minerals, Nomenclature and Classification (CNMNC) of the IMA, of which just over 435 occur in meteorites (Rubin and Ma 2017). The recent surge in new mineral discoveries from meteorites is largely the result of detailed high-spatial-resolution analytical SEM, EPMA, TEM and synchrotron XRD investigations (Ma et al. 2012, 2013, 2020; Ma 2015, 2018; Rubin and Ma 2017). These new mineral discoveries reveal the myriad of processes recorded by minerals in meteorites that span the history of our Solar System and before. A more complete inventory of mineral phases in meteorites can help resolve formational processes in planetesimals in greater detail and, thus aids our exploration of the Solar System and beyond.

Acknowledgements

We are grateful to the staff and for use of the facilities in the John M. Cowley Center for High Resolution Electron Microscopy at Arizona State University. We thank the editor Simon Redfern and Michael Zolensky and Thomas Zega for their timely reviews which helped improve the quality of the paper.

Funding

This work was in part funded by a NASA Emerging Worlds grant NNX17AE56G to L.A.J.G and supported in part by NASA Earth and Space Science Fellowship (NESSF) award 80NSSC18K1269 to S.R. and M.W. EBSD and EPMA were carried out at the Caltech GPS Division Analytical Facility, which is supported in part by NSF grants EAR-0318518 and DMR-0080065.

References Cited

Beck, U., Neumann, H.G., and Becherer, G. (1973) Phasenbildung in Ni/Si-Schichten. Kristall und Technik, 8, 1125-1129.

Buchwald, V.F. (1975) Handbook of iron meteorites. Arizona State University, Center for Meteorite Studies, and University of California Press, Berkeley, 3 vol, 1426 pp.

Casanova, I., Keil., K. and Newsom, H.E. (1993) Composition of metal in aubrites: Constraints on core formation. Geochimica et Cosmochimica Acta, 57, 675-682.

Garvie, L.A.J., Wittmann, A., Ray, S. and Wadhwa, M. (2017) Elemental and structural diversity in Norton County metal nodules. 80th Annual Meeting of the Meteoritical Society 2017 (LPI Contrib. No. 1987). Abstract #6384.

Garvie, L.A.J., Ray, S., Wadhwa, M., Wittmann, A., and Domanik, K. (2018) Scrutinizing six silicide-bearing samples of metal from the Norton County aubrite. 49th Lunar and Planetary Science Conference 2018 (LPI Contrib. No. 2083). Abstract #2104.

Goldstein, J.I., Yang, J., Kotula, P.G., Michael, J.R., and Scott, E.R.D. (2009) Thermal histories of IVA iron meteorites from transmission electron microscopy of the cloudy zone microstructure. Meteoritics and Planetary Science, 44, 343-358.

Keil, K. (2010) Enstatite achondrite meteorites (aubrites) and the histories of their asteroidal parent bodies. Chemie der Erde, 70, 295-317.

Keil, K., Berkley, J.L. and Fuchs, L.H. (1982) Suessite, Fe_3Si: a new mineral in the North Haig ureilite. American Mineralogist 67, 126-131

La Paz, L. (1948) The achondritic shower of February 19, 1948. Publication of the Astronomical Society of the Pacific, 61, 63-73.

Lashko, N.F. (1951) On the phase diagram of Ni-Si. Doklady Akademii Nauk SSSR, 81, 606-607.

Leonard, F.C. (1948) The Furnas County stone of the Norton County, Kansas-Furnas County Nebraska, achondritic fall. Popular Astronomy, 56, 434-436.

Ma, C. (2015) Nanomineralogy of meteorites by advanced electron microscopy: Discovering new minerals and new materials from the early solar system. Microscopy and Microanalysis, 21 (S3), paper No. 1175, 2353-2354.

Ma, C. (2018) A closer look at shocked meteorites: Discovery of new high-pressure minerals. American Mineralogist, 103, 1521-1522.

Ma, C. and Rossman, G.R. (2008) Barioperovskite, $BaTiO_3$, a new mineral from the Benitoite Mine, California. American Mineralogist, 93, 154-157.

Ma, C. and Rossman, G.R. (2009) Tistarite, Ti_2O_3, a new refractory mineral from the Allende meteorite. American Mineralogist, 94, 841-844.

Ma, C., Tschauner, O., Beckett, J.R., Rossman, G.R., and Liu, W. (2012) Panguite, $(Ti^{4+},Sc,Al,Mg,Zr,Ca)_{1.8}O_3$, a new ultra-refractory titania mineral from the Allende meteorite: Synchrotron micro-diffraction and EBSD. American Mineralogist, 97, 1219-1225.

Ma, C., Tschauner, O., Beckett, J.R., Rossman, G.R., and Liu, W. (2013) Kangite, $(Sc,Ti,Al,Zr,Mg,Ca,\square)_2O_3$, a new ultrarefractory scandia mineral from the Allende meteorite: Synchrotron micro-Laue diffraction and electron backscatter diffraction. American Mineralogist, 98, 870-878.

Ma, C., Krot, A.N., Beckett, J.R., Nagashima, K., Tschauner, O., Rossman, G.R., Simon, S.B., and Bischoff, A. (2020) Warkite, $Ca_2Sc_6Al_6O_{20}$, a new mineral in carbonaceous chondrites and a key-stone phase in ultrarefractory inclusions from the solar nebula. Geochimica et Cosmochimica Acta, 277, 52-86.

Ochiai, S., Mishima, Y., and Suzuki, T. (1984) Lattice parameter data of Ni (gamma), Ni_3Al (gamma) and Ni_3Ga (gamma) solid solutions. Bulletin of Research Laboratory of Precision Machinery and Electronics (Tokyo Institute of Technology), 53, 15-28.

Okada, A., Kobayashi, K., Ito, T., Sakurai, T. (1991) Structure of synthetic perryite, $(Ni,Fe)_8(Si,P)_3$. Acta Crystallographica, C47, 1358-1361.

Pouchou, J.-L. and Pichoir, F. (1991) Quantitative analysis of homogenous or stratified microvolumes applying the model "PAP", in Heinrich, K.F.J., and Newbury, D.E. Electron Probe Quantitation, p. 31-75, Plenum Press, New York.

Rabadanov, M.Kh. and Ataev, M.B. (2002) Atomic scattering and enormous anisotropy of thermal expansion in NiSi single crystals. I. Refinement of structure models. Kristallografiya, 47, 40-45.

Ray, S., Wadhwa, M., Rai, V.K. (2019a) Iron isotope compositions of large metal nodules from the Norton County aubrite. 50th Lunar and Planetary Science Conference (LPI Contrib. No. 2132). Abstract #1960.

Ray, S., Wadhwa, M., Rai, V.K. and Garvie, L.A.J. (2019b) Iron isotope compositions of Si-bearing metal nodules from the Mount Egerton aubrite. 82nd Annual Meeting of the Meteoritical Society 2019 (LPI Contrib. No. 2157). Abstract #6427.

Ray, S., Garvie, L.A.J., Rai, V.K. and Wadhwa, M. (2020) Correlated iron isotopes and silicon in aubrite metals reveal structure of their asteroidal parent body. Nature Communications, in prep.

Ross, A.J., Downes, H., Herrin, J.S., Mittlefehldt, D.W., Humayun, M. and Smith, C., (2019) The origin of iron silicides in ureilite meteorites. Geochemistry, 79, 125539.

Rubin, A.E. and Ma, C. (2017) Meteoritic minerals and their origins. Chemie der Erde, 77, 325-385.

Santamaria-Perez, D., Nuss, J., Haines, J., Jansen, M. and Vegas, A. (2004) Iron silicides and their corresponding oxides: a high-pressure study of Fe_5Si_3. Solid State Sciences, 6, 673-678.

Schuette, M., Wartchow, R. and Binnewies, M. (2003) Shape controlling synthesis - formation of Fe_3Si by the reaction of iron with silicon tetrachloride and crystal structure refinement. Zeitschrift für Anorganische und Allgemeine Chemie, 629, 1846-1850.

Toman, K. (1952) The structure of Ni_2Si. Acta Crystallographica, 5, 329-331.

Wai, C.M. (1970) The metal phase of Horse Creek, Mount Egerton, and Norton County enstatite meteorites. Mineralogical Magazine, 37, 905-908.

Wasson, J.T. and Wai, C.M. (1970) Composition of the metal, schreibersite and perryite of enstatite achondrites and the origin of enstatite chondrites and achondrites. Geochimica et Cosmochimica Acta, 34, 169-184.

Yang, C.-W., Williams, D.B. and Goldstein, J.I. (1997) Low-temperature phase decomposition in metal from iron, stony-iron, and iron meteorites, Geochimica et Cosmochimica Acta, 61, 2943-2956.

Yang, J. and Goldstein, J.I. (2005) The formation of the Widmanstätten structure in meteorites. Meteoritics and Planetary Science, 40, 239-253.

Zhang, J., Williams, D.B. and Goldstein, J.I. (1993) The microstructure and formation of duplex and black plessite in iron meteorites. Geochimica et Cosmochimica Acta, 57, 3725-3735.

Table 1. Average elemental composition determined by EPMA for the type carletonmooreite (Caltech data). All data from the grains associated with plessite Pl1. Analyses in wt%.

Element	**Mean (n=6)**	**Range**	**S.D.**
Ni	82.80	82.23-83.47	0.40
Fe	4.92	4.78-5.02	0.09
Si	13.08	12.97-13.18	0.08
Total	100.81		

Table 2. Carletonmooreite electron microprobe analyses (ASU data) of crystals from the triangular (Pl1) and flashlight-shaped (P12) plessite. Analyses in wt%.

Element	**Pl1a (n=3)**	**Pl1b**	**Pl1c**	**Pl1d**	**Pl2a (n=3)**	**Pl2b (n=2)**
Si	13.08±0.04	13.16	12.99	12.89	13.02±0.06	12.90±0.05
Fe	4.83±0.06	5.19	6.09	5.68	6.36±0.12	7.29±0.35
Cu	0.11±0.02	0.15	0.13	0.14	0.14±0.02	0.11±0.01
Ni	82.35±0.61	81.44	81.20	81.80	81.26±0.19	80.29±0.74
Total	100.38±0.56	99.94	100.40	100.50	100.79±0.31	100.59±0.44

This is the peer-reviewed, final accepted version for American Mineralogist, published by the Mineralogical Society of America.
The published version is subject to change. Cite as Authors (Year) Title. American Mineralogist, in press.
DOI: https://doi.org/10.2138/am-2021-7645. http://www.minsocam.org/

Table 3. Electron microprobe analyses (wt%) of carletonmooreite and surrounding phases in the Norton County metal nodule (NC12).

Element	**carletonmooreite**			**bulk metal (195)**	**kamacite (50)**	**perryite[1] (6)**	**schreibersite range**
	Pl1-Caltech (6)	**Pl1-ASU (6)**	**Pl2-ASU (5)**				
Fe	4.92±0.09	5.24±0.53	6.73±0.55	90.48	93.4	1.09	50.77 – 32.38
Ni	82.80±0.40	81.91±0.64	80.87±0.66	8.10	5.83	82.80	33.68 – 52.80
Cu	n.a.*	0.13±0.02	0.13±0.02	b.d.l.	b.d.l.	0.34	b.d.l.
Co	b.d.l.**	b.d.l.	b.d.l.	0.30	0.32	n.d.	0.13 – 0.03
Cr	b.d.l.	b.d.l.	b.d.l.	b.d.l.	b.d.l.	b.d.l.	b.d.l.
Si	13.08±0.08	13.08±0.10	12.98±0.08	0.73	0.40	13.07	0.08 – 0.11
P	b.d.l.	b.d.l.	b.d.l.	0.10	b.d.l.	2.72	15.65 – 15.61
Total	100.81	100.54±0.41	100.94±0.33	99.71	99.95	100.02	100.37 – 100.99

* n.a. – not analyzed. ** b.d.l. – below detection limit by WDS. [1]perryite analyses from grains extracted from Norton County metal nodule NC9.

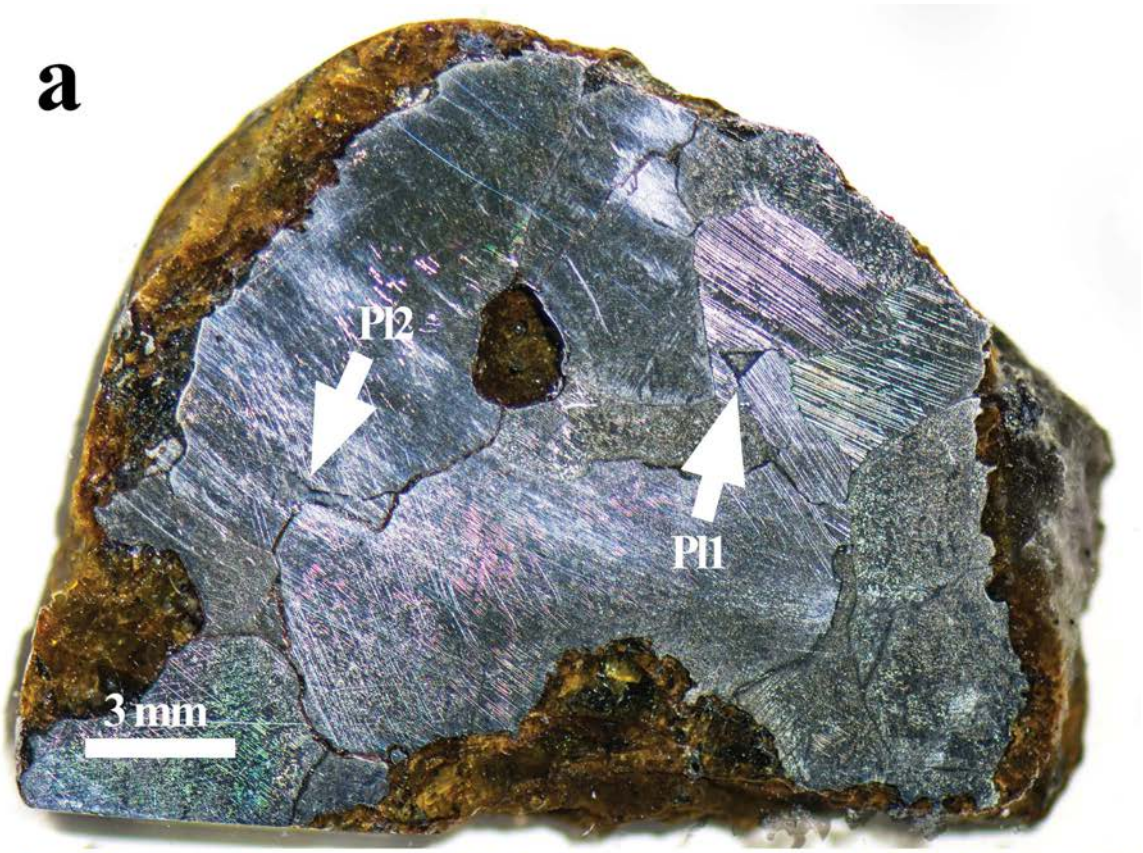

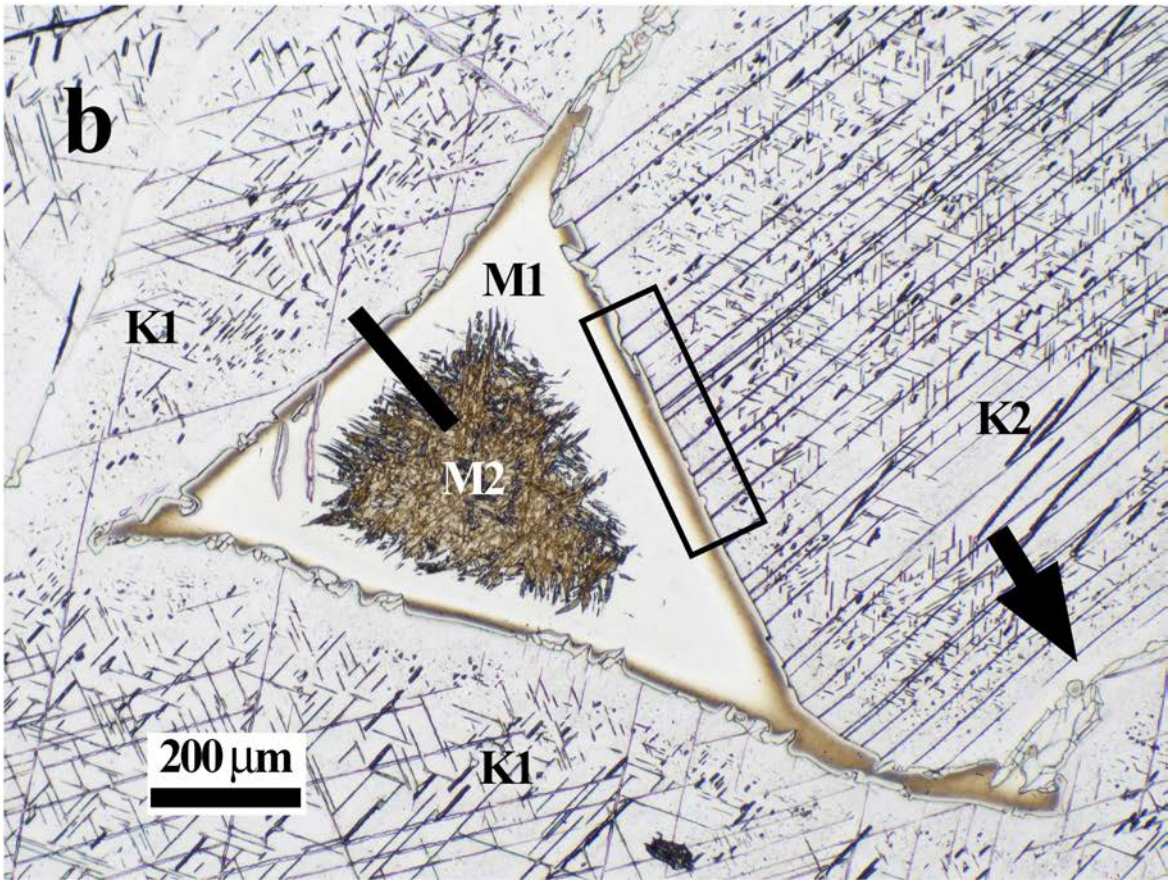

Figure 1. **a**) Photograph of a polished and nital etched section through Norton County nodule NC12. The white arrows point to the plessitic regions P11 and P12. The metal is surrounded by brown-stained enstatite and contains a rounded 2-mm-sized bleb of enstatite. **b**) Reflected-light photograph of the triangular plessitic structure (Pl1) surrounded by kamacite (two grains K1 and K2). The fine lines in the kamacite are from Neumann bands and perryite revealed through the nital etching. The plessite has a complex structure consisting of several elementally distinct layers (rectangular region shown at higher magnification in Fig. 2a), clear taenite (M1) surrounding dark etched taenite (M2). The thick black line shows the location of the element map in Fig. 3a. Black arrow point to schreibersite stringers.

This is the peer-reviewed, final accepted version for American Mineralogist, published by the Mineralogical Society of America.
The published version is subject to change. Cite as Authors (Year) Title. American Mineralogist, in press.
DOI: https://doi.org/10.2138/am-2021-7645. http://www.minsocam.org/

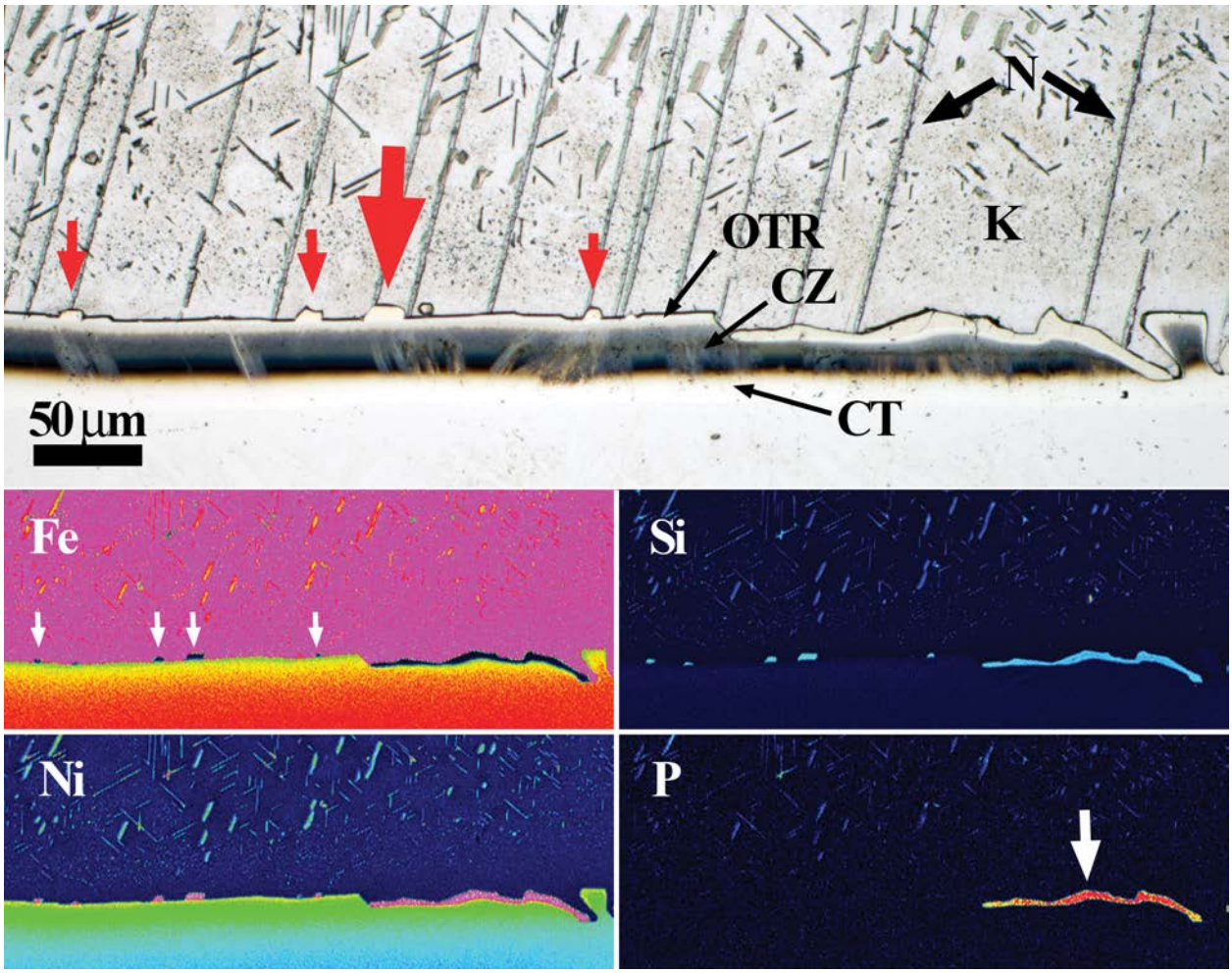

Figure 2. **Top panel:** Optical, reflected-light image of the rectangular region in Fig. 1b showing the locations of the carletonmooreite crystals (red arrows) attached to tetrataenite labelled OTR (outer taenite rim). The large red arrow indicates the crystal probed for the EBSD analysis in figure 4. CZ – cloudy zone. CT – clear taenite. N – Neumann bands. K – kamacite. **Lower panels**: The four false-color images show element maps for Fe, Ni, Si, and P and show the same area as the top panel. The white arrows in the Fe map point to the same areas as the red arrows in the top panel. The arrow in the P panel points to a perryite grain. Carletonmooreite is distinguished from the perryite in being free of P.

This is the peer-reviewed, final accepted version for American Mineralogist, published by the Mineralogical Society of America.
The published version is subject to change. Cite as Authors (Year) Title. American Mineralogist, in press.
DOI: https://doi.org/10.2138/am-2021-7645. http://www.minsocam.org/

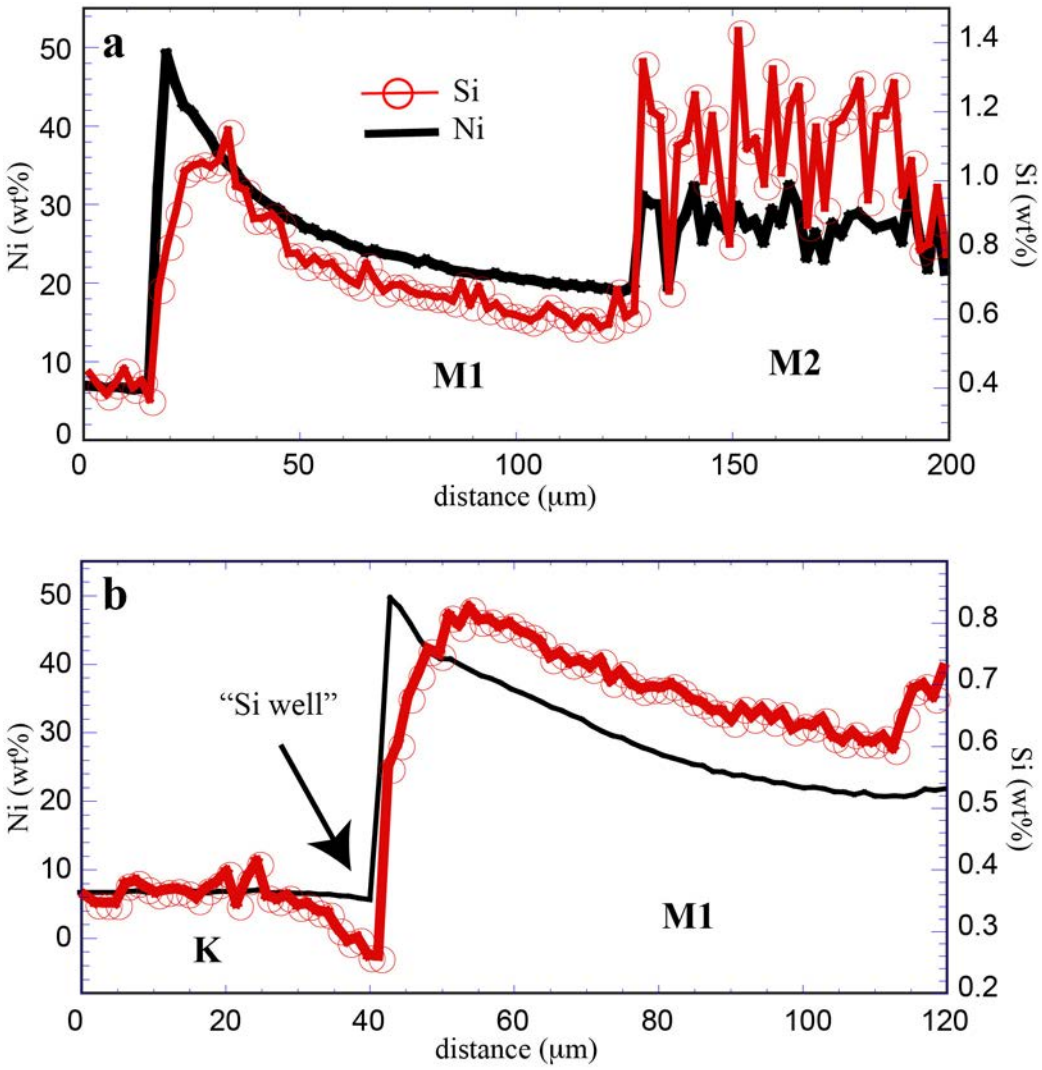

Figure 3. The elemental profiles for Ni and Si from kamacite (K) and across the tetrataenite boundary into plessite. **a**) Element profiles from the kamacite into the center of plessite (Pl1). M1 – clear taenite, M2 – cloudy taenite. **b**) Element profiles across the kamacite/plessite (Pl2) boundary showing the "Si-well". Location of this boundary is shown as a white line in Figure S2.

This is the peer-reviewed, final accepted version for American Mineralogist, published by the Mineralogical Society of America.
The published version is subject to change. Cite as Authors (Year) Title. American Mineralogist, in press.
DOI: https://doi.org/10.2138/am-2021-7645. http://www.minsocam.org/

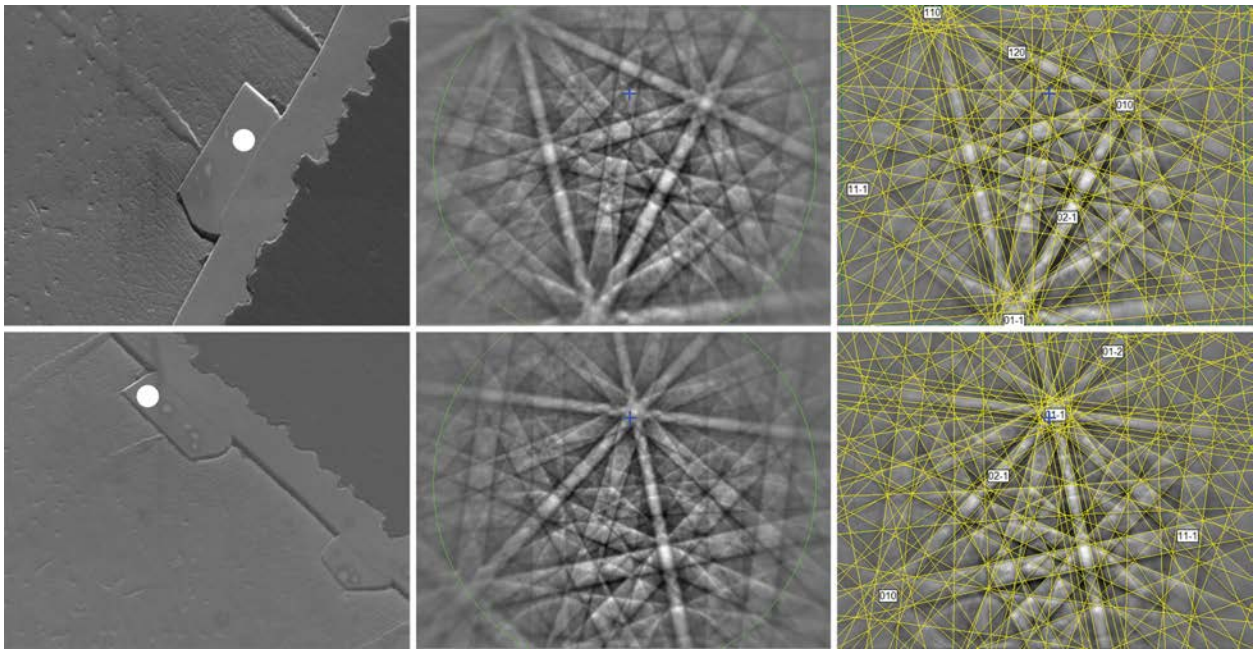

Figure 4. **Left column**: Secondary electron image (SEI) of the largest carletonmooreite crystal (large red arrow in Fig. 2a) in two orientations. The white circle shows the location where the EBSD patterns were measured. **Middle column**: EBSD patterns recorded from the two orientations. **Right column**: Patterns indexed with the *Pm-3m* Ni_3Si structure.

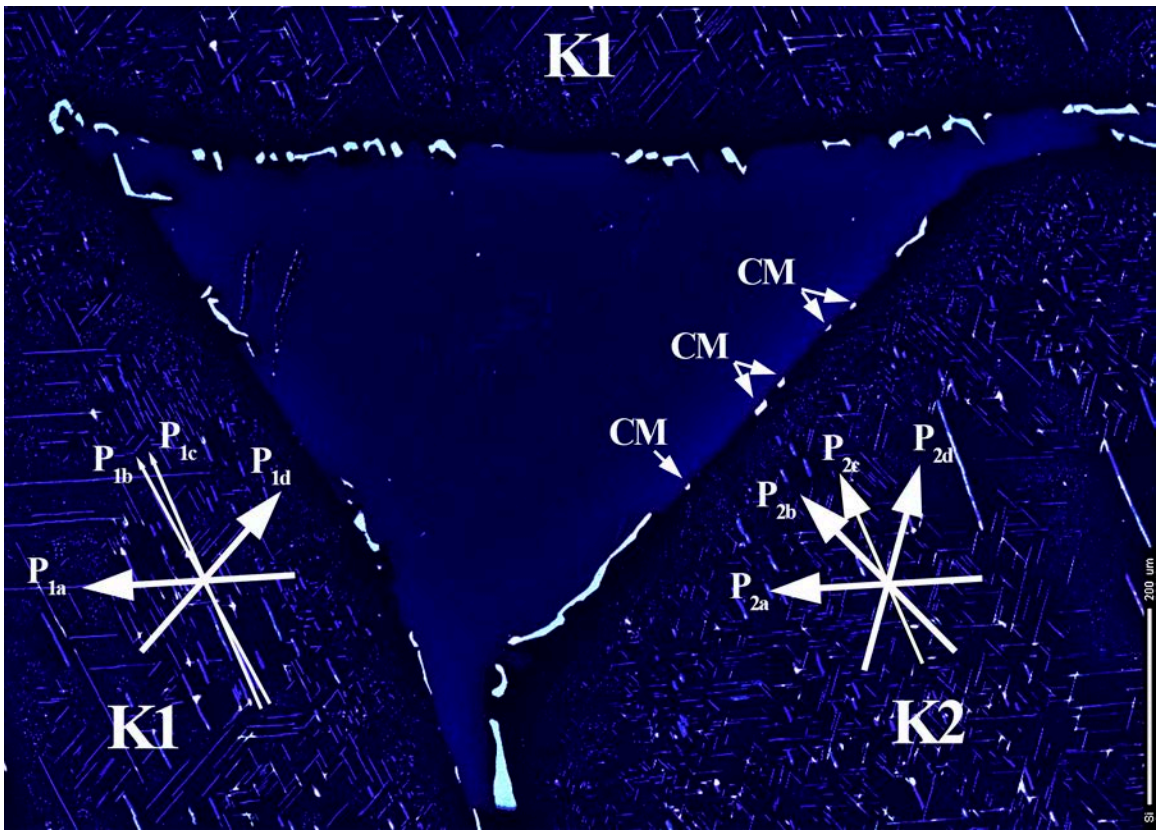

Figure 5. False-color Si x-ray map of the plessite triangle and surrounding kamacite. High Si shown as white and low as black. Silicon occurs primarily in perryite, carletonmooreite (CM), and high Ni-metal. The plessite is surrounded by two kamacite grains in different orientations - K1 and K2, which are also shown in Fig. 1b. Perryite shows four orientations P_{1a} to P_{1d} and P_{2a} to P_{2d} in kamacite grains K1 and K2, respectively. The arrows show the directions of the perryite laths.

This is the peer-reviewed, final accepted version for American Mineralogist, published by the Mineralogical Society of America.
The published version is subject to change. Cite as Authors (Year) Title. American Mineralogist, in press.
DOI: https://doi.org/10.2138/am-2021-7645. http://www.minsocam.org/

Supplementary Figures and Tables

Carletonmooreite, Ni_3Si, a new silicide from the Norton County, aubrite meteorite

Laurence A.J. Garvie[1,2], Chi Ma[3], Soumya Ray[2], Kenneth Domanik[4], Axel Wittmann[5], and Meenakshi Wadhwa[2].

[1]Center for Meteorite Studies, [2]School of Earth and Space Exploration, Arizona State University, 781 East Terrace Rd., Tempe, AZ 85287-6004, USA (lgarvie@asu.edu). [3]Division of Geological and Planetary Sciences, California Institute of Technology, 1200 East California Boulevard, Pasadena, CA 91125, USA, [4]Lunar and Planetary Laboratory, University of Arizona, 1415 N 6th Ave, Tucson, AZ 85705,[5]Eyring Materials Center, Arizona State University, Tempe, AZ 85287, USA.

This is the peer-reviewed, final accepted version for American Mineralogist, published by the Mineralogical Society of America.
The published version is subject to change. Cite as Authors (Year) Title. American Mineralogist, in press.
DOI: https://doi.org/10.2138/am-2021-7645. http://www.minsocam.org/

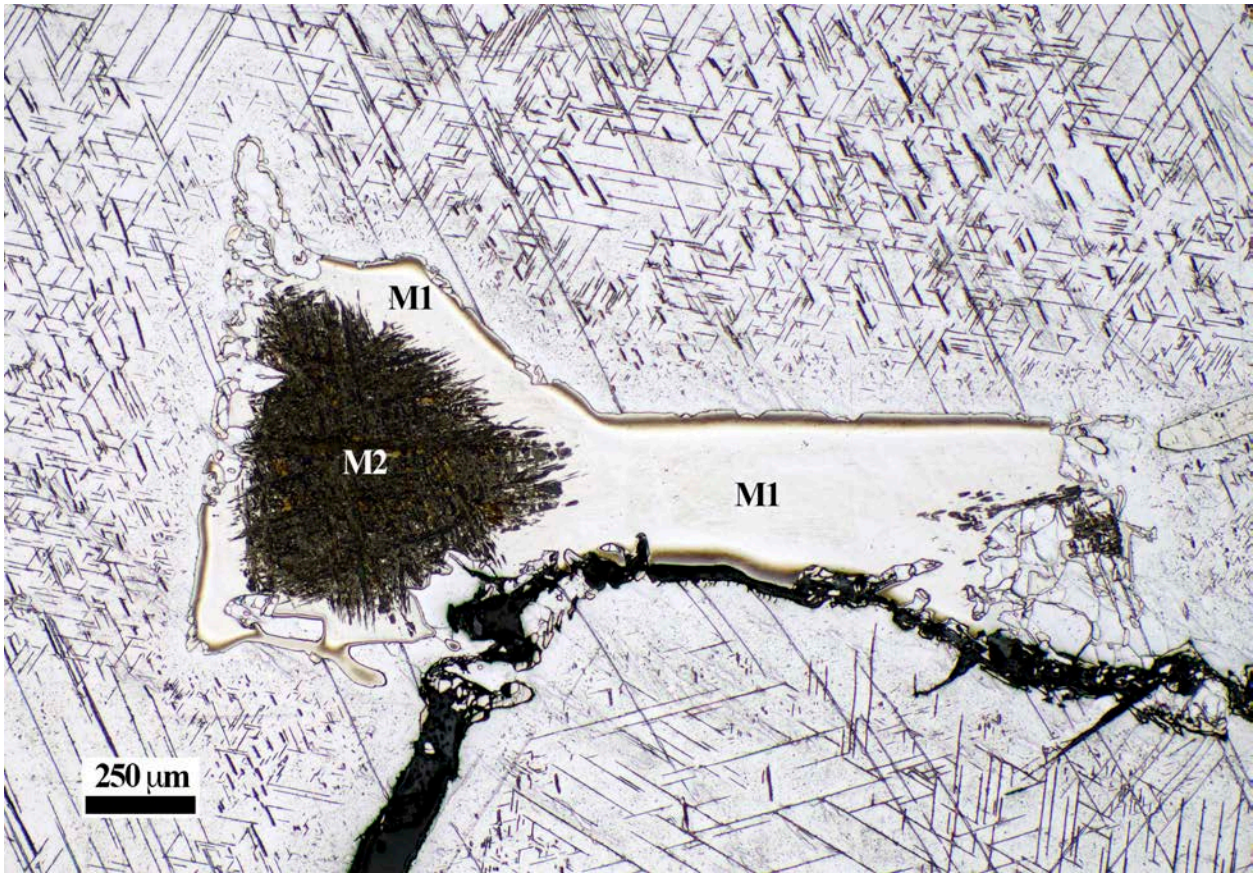

Figure S1. Reflected-light photograph of the flashlight-shaped plessitic structure (Pl2) surrounded by kamacite. The fine lines in the kamacite is from Neumann bands and perryite revealed through the nital etching. The plessite has a complex structure consisting of several elementally distinct layers, clear taenite (M1) surrounding dark etched taenite (M2).

This is the peer-reviewed, final accepted version for American Mineralogist, published by the Mineralogical Society of America.
The published version is subject to change. Cite as Authors (Year) Title. American Mineralogist, in press.
DOI: https://doi.org/10.2138/am-2021-7645. http://www.minsocam.org/

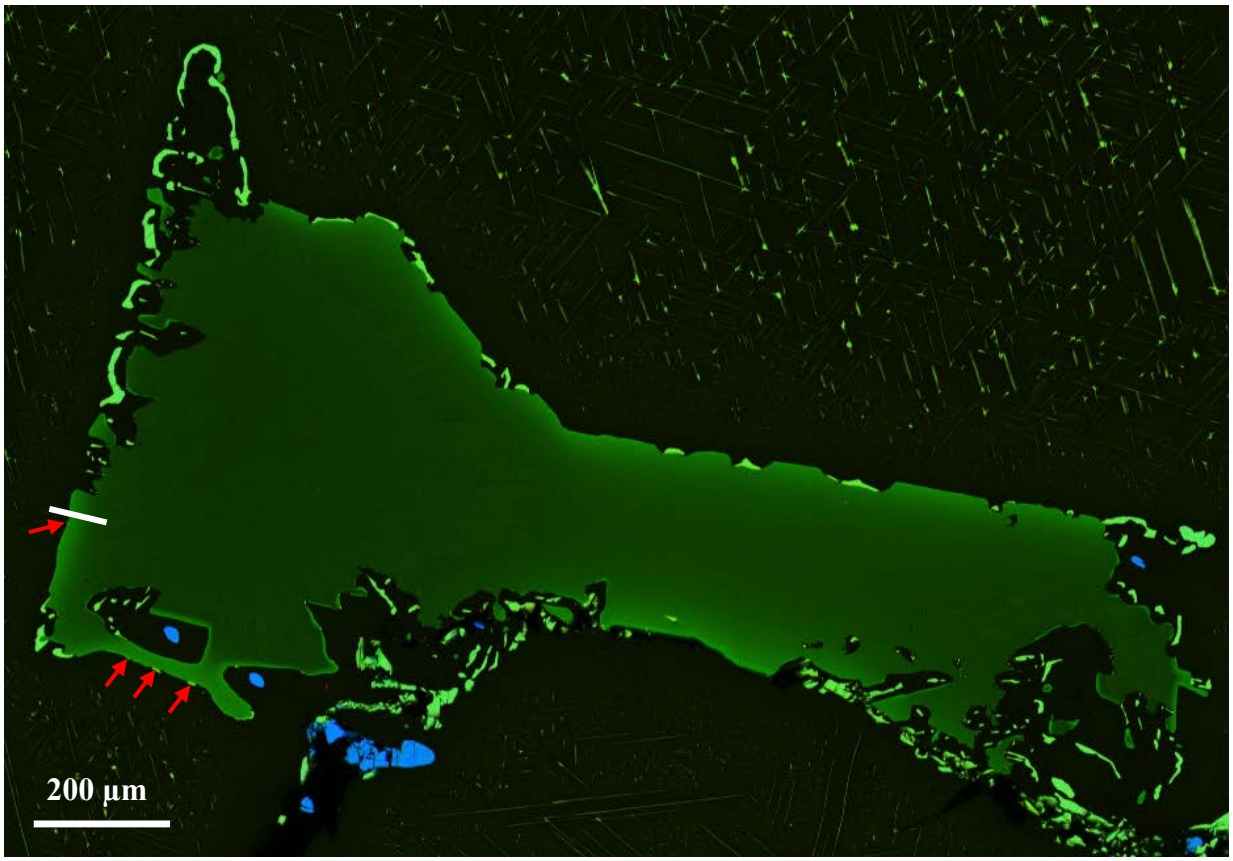

Figure S2. Composite WDS X-ray intensity map of the plessite Pl2 (Red-Si, Green-Ni, Blue-P). Red arrows point to carletonmooreite crystals. White line is the location of the WDS traverse show in Figure 3b. Blue grains are schreibersite.

This is the peer-reviewed, final accepted version for American Mineralogist, published by the Mineralogical Society of America.
The published version is subject to change. Cite as Authors (Year) Title. American Mineralogist, in press.
DOI: https://doi.org/10.2138/am-2021-7645. http://www.minsocam.org/

Table S1. Calculated X-ray powder diffraction data for carletonmooreite ($I_{rel} > 1$).

h	*k*	*l*	*d* [Å]	I_{rel}
1	0	0	3.5100	8
1	1	0	2.4819	7
1	**1**	**1**	**2.0265**	**100**
2	**0**	**0**	**1.7550**	**49**
2	1	0	1.5697	4
2	1	1	1.4330	3
2	**2**	**0**	**1.2410**	**31**
2	2	1	1.1700	1
3	1	0	1.1100	1
3	**1**	**1**	**1.0583**	**34**
2	**2**	**2**	**1.0133**	**10**
3	2	0	0.9735	1
3	2	1	0.9381	1
4	0	0	0.8775	4
3	**3**	**1**	**0.8053**	**11**
4	**2**	**0**	**0.7849**	**10**
4	2	2	0.7165	7
5	1	1	0.6755	5
3	3	3	0.6755	2
4	4	0	0.6205	2
5	3	1	0.5933	6
6	0	0	0.5850	1
4	4	2	0.5850	3